batteries

MDPI

Article

Metal-Organic Frameworks (MOFs)-Integrated Separator for Improving the Cycle Stability of Lithium–Ion Batteries

Apurba Ray [1,*], Neil Wood [1], Emre Guney [2], Bilal Tasdemir [1], Kamil Burak Dermenci [2], Maitane Berecibar [2] and Bilge Saruhan [1,3,*]

[1] Institute for Frontier Materials on Earth and in Space, German Aerospace Center (DLR e.V.), Linder Hoehe, 51147 Cologne, Germany
[2] MOBI-Electromobility Research Centre, Department of Electrical and Energy Technology, Vrije Universiteit Brussel, Pleinlaan 2, 1050 Brussels, Belgium
[3] Department of Materials Science Technologies, Faculty of Sciences, Turkish-German University, Sahinkaya Cad. 106, Beykoz, 34820 Istanbul, Türkiye
* Correspondence: apurba.ray@dlr.de (A.R.); bilge.saruhan@dlr.de (B.S.)

Abstract

To date, lithium–ion batteries (LIBs) are considered one of the most promising and market-leading energy storage systems due to their high theoretical capacity and energy density. However, poor thermal and cyclic stability, low electrolyte uptake, and the possibility for frequent short circuits of typical separators and evolution of several gases during long cycle operation pose several problems for LIBs. Metal-organic frameworks (MOFs) have attracted widespread interest as a promising material for improving the cycle stability and safety of rechargeable batteries due to their inherent surface and structural properties such as high specific surface area, high porosity, and ionic conductivity. In this work, the aim is to provide detailed descriptions of the synthesis routes and parameters for obtaining various MOFs such as Zr-MOF-808 and Ni-MOF-74 nanoparticles and the fabrication of those MOF-integrated separators. To optimize the crystallinity, morphological and compositional characteristics, and several material characterizations such as XRD, SEM, and EDX have been applied. Afterwards, the synthesized MOF-integrated glass fiber (GF) separators have been developed for lithium–ion battery (LIB) applications. To investigate the electrochemical performance and the effect of MOF integration into the separators, electrochemical studies in the form of galvanostatic charge–discharge (GCD), electrochemical impedance spectroscopy (EIS) have been evaluated by preparing CR2032-type half-coin cells. This MOFs-integrated GF-separators and synthesized $LiNi_{0.6}Mn_{0.2}Co_{0.2}O_2$ (NMC622) cathode materials-based coin cell LIB exhibited higher cycle stability than bare GF-separator based LIB. This novel approach and extensive research suggest that development of MOF-integrated separators could significantly improve cycle stability by reducing the internal cell degradation for next generation energy storage devices.

Keywords: energy storage; lithium–ion batteries; MOFs; separators; cycle stability

Academic Editor: Zhenbo Wang

Received: 25 May 2026
Revised: 9 June 2026
Accepted: 13 June 2026
Published: 16 June 2026

1. Introduction

Lithium ion batteries (LIBs) are considered as one of the most market leading energy storage systems with the application in electric vehicles (EVs) and various portable electronics [1–3]. However, emerging electric vehicles are looking for further improvements in LIBs' power density, lifecycle, safety, and minimal cell degradation. In general, the uncontrolled volume expansion and formation of lithium-dendrites limits the commercialization of

lithium–metal anodes [4,5]. During the charge–discharge process of LIBs, the Li-metal anode comes into contact with the electrolyte and forms a solid electrolyte interface (SEI) layer on the surface of the Li-anode through chemical reactions. As a result, this SEI layer cannot prevent the further growth of Li-dendrites and at the same time causes a rapid increase in the interfacial resistance between the separator and the anode [6,7]. According to the literature, thermal runaway and various types of gas evolution are also major issues in LIB cells, particularly under abusive operating conditions such as overcharging, extreme temperatures, and cell deformations [8–10]. Gas evolution in LIBs occurs from multiple sources, including decomposition of electrolyte solvents and the structural deformation of cathode materials [10,11]. Specially, during the initial formation cycle, gas is primarily generated through electrolyte decomposition and O^{2-} release from cathode oxidation [12]. Such gas evolution has a profound impact on battery performance, such as electrode degradation, volume expansion, reduced shelf life, increased cell impedance, reduced cycle life, electrolyte displacement, and safety issues [4,13]. The evolution of degradative gases strongly depends on the electrode–electrolyte composition and the operational voltage window of the cell. Nevertheless, performance and energy density of the LIB remains a popular research topic. Among the various strategies to increase the specific capacity ($\geq$200 mAh/g) and cycle lifetime (>1200 cycles) of LIBs over a wide voltage range, increasing the fraction of highly redox-active Ni in $Li_{1+x}(Ni_{1-y-z}Mn_yCo_z)_{1-x}O_2$ (NMC) cathode materials (such as Ni-rich $LiNi_{0.8}Mn_{0.1}Co_{0.1}O_2$ (NMC811), $LiNi_{0.9}Mn_{0.05}Co_{0.05}O_2$ (NMC90)) offers a highly effective solution [1,14,15]. However, the long charge–discharge process, lattice disordering (Jahn–Teller) of manganese ions, dissolution of metal ions such as nickel ions, and the evolution of several gases due to unwanted side reactions also cause lower capacity retention. Furthermore, the operation of NMC cathode in liquid electrolyte-based LIBs results in the evolution of several gases such as H_2, O_2, CO, CO_2, and relative humidity (H_2O) [10,16]. The specific causes of gas evolution are the electrochemical oxidation of organic electrolytes, electrochemical decomposition of residual Li_2CO_3 species formed on the surface of Ni-rich NMC cathodes and structural instability of NMC cathodes at high state of charge (SOC) [17,18].

To address the aforementioned issues in battery systems, numerous efforts have been devoted worldwide to developing new materials and battery chemistries to improve battery cycle life without compromising battery performance [6,19]. Modern research also shows that many of the issues can be relatively easily resolved or mitigated by improving the performance of battery separators rather than modifying anode, cathode, or electrolyte materials. Separator, one of the most important components of battery technology, prevents direct electrical contact between anode and cathode and provides a favorable channel for ion transport towards the electrodes [6,7,20]. Commercial separators such as polyethylene (PE), polypropylene (PP), etc., have very good electrochemical stability, good mechanical stability, and low price. However, the low porosity, low thermal stability and selective electrolyte wettability of these commercial separators lead to high cell impedance, low energy density and reduced Li-ion transport rate, which significantly affects the long cycle stability and rate performance of LIBs [21]. To overcome the above-mentioned problems of unwanted gas evolution, low thermal stability and poor electrolyte wettability of commercial separators in LIBs, various approaches have been proposed [22]. Among these, metal-organic frameworks (MOFs) have attracted a great interest in recent years as new materials for gas adsorbents, gas removal/storage, heterogeneous catalysis, ion exchange, and molecular separation [23,24]. The high tunability in design, large void spaces, ultra-high active surface areas, crystalline nature and extensive structural and chemical diversity of MOFs make them one of the fastest growing materials, which has encouraged researchers to use them in multiple applications [25,26]. MOFs have also proven themselves

as alternatives to several gas absorbents and storage-capable multifunctional components to improve the battery life of LIBs under abuse conditions [27]. The development of novel porous MOFs-integrated separators has become one of the most important research interests for high performance batteries applications [7,28,29]. An inherently well-ordered porous structure of MOF-nanoparticles makes them promising materials for improving the safety and cycle stability of lithium–ion batteries. Among several MOFs materials, Zr and Ni-based MOFs exhibit excellent ion adsorption capacities and efficient ion sieving properties for above mentioned gases [30–33].

In this work, Zr-MOF and Ni-MOF nanoparticles have been synthesized via a simple and cost-effective solvothermal method. In order to improve the cycle stability of LIBs, the synthesized Zr-MOF and Ni-MOF nanoparticles have been integrated into glass fiber (GF) separators and assembled into LIBs to investigate the battery performance. The MOF-integrated GF separator and NMC622 cathode material-based LIBs exhibit higher cycle stability than that of bare GF-separator based LIB. While several studies and reviews have explored metal-organic framework (MOF)-modified separators for energy storage applications, primarily lithium–sulfur batteries, a comprehensive, comparative study on MOF-integrated separators specifically for lithium–ion batteries remains absent from the literature. To bridge this gap, this work presents the first detailed comparative investigation of two distinct types of MOFs integrated into glass fiber (GF) separators. This unique research offers a novel strategy for enhancing the performance of next-generation energy storage systems.

2. Materials and Methods

Zirconium (IV) tetrachloride ($ZrCl_4$, Merck KGaA, 98%, Darmstadt, Germany), nickel nitrate hexahydrate ($Ni(NO_3)_2$ $6H_2O$, Carl Roth GmbH + Co. KG, 98%, Karlsruhe, Germany), N, N-dimethylformamide (DMF) (Merck KGaA and 99%), formic acid (CH_2O_2, AppliChem GmbH, 98%, Darmstadt, Germany), benzene-1,3,5-tricarboxylic acid (BTC, Thermo Fisher Scientific Inc., 98%, Waltham, MA, USA), methanol (CH_4O, Th. Geyer GmbH & Co. KG, 99.9%, Renningen, Germany,), 2,5-dihydroxyterephthalic acid (DHTPA, Fluorochem Limited 95%, Hadfield, UK), nickel (II) acetate tetrahydrate ($Ni(CH_3COO)_2$ $4H_2O$, chemPUR, 99%, Karlsruhe, Germany,), manganese (II) acetate tetrahydrate ($Mn(CH_3COO)_2$ $4H_2O$, Carl Roth, ≥99%), Cobalt (II) acetate tetrahydrate ($Co(CH_3COO)_2$ $4H_2O$, Carl Roth, ≥98%), lithium acetate ($Li(CH_3COO)$, BLD Pharmatech Ltd. ≥99%, Shanghai, China), and oxalic acid ($C_2H_2O_4$ $2H_2O$, Glentham Life Sciences, 98%, Corsham, UK) were purchased and used without further purification for synthesis of the materials.

2.1. Synthesis of Zr-MOF-808 Through Solvothermal Synthesis Route

The Zr-MOF-808 was synthesized through an easy and cost-effective solvothermal synthesis. A suitable amount of zirconium (IV) tetrachloride ($ZrCl_4$) (0.15 mmol) was first dissolved in a 15 mL N, N-dimethylformamide (DMF) solution. Then, 15 mL of formic acid (CH_2O_2) and 0.2 mmol of Benzene-1,3,5-tricarboxylic acid (BTC) or trimesic acid were slowly added to the solution. Finally, 0.5 mL of distilled water was added to the mixed solution as a modulator agent. The final mixture of precursors was kept for 24 h at a constant temperature of 120 °C in a 100 mL screw-capped glass bottle. Afterwards, the white color precipitated materials were washed several times with DMF and methanol solution to remove the residual reagents. The precipitated materials were then dried at 80 °C overnight to get the final powder sample of Zr-MOF-808 ($Zr_6(OH)_4(BTC)_2(COOH)_6$). The possible chemical reaction has been represented in Figure 1.

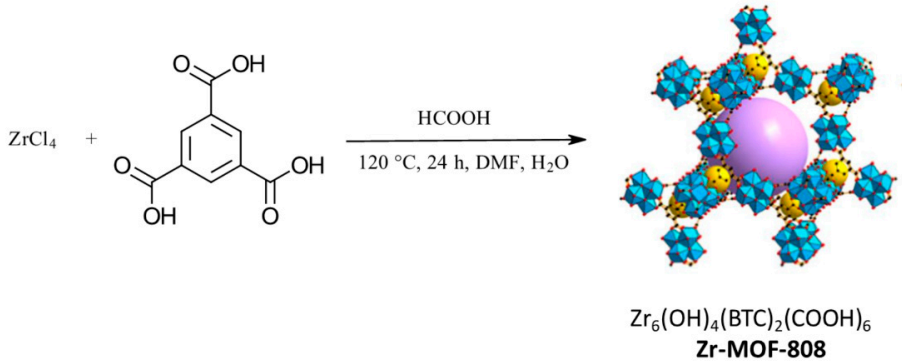

Figure 1. Possible precipitation reaction in Zr-MOF-808 synthesis through the solvothermal process.

2.2. Synthesis of Ni-MOF-74 Through the Solvothermal Synthesis Route

The Ni-MOF-74 materials was also synthesized by following simple and cost-effective solvothermal synthesis. For this synthesis, 1.2 mmol nickel nitrate hexahydrate ($Ni(NO_3)_2$ $6H_2O$) and 0.5 mmol 2,5-dihydroxyterephthalic acid (DHTPA) were added to 30 mL of a mixture of 15:1:1 ($v/v/v$) DMF-ethanol-water. This solution was then sonicated in an ultrasonic bath for approx. 1 h until the precursors had completely dissolved. The reaction solution was then filled into an autoclave Teflon reactor and placed in an oven for 24 h at 100 °C. After cooling to room temperature, the precipitated mixture was transferred and the precipitated brownish solid was washed three times with 30 mL of DMF and three times with 30 mL of methanol. After filtration, the sample was dried in a vacuum oven for 16 h overnight at 80 °C. The product Ni-MOF-74 was obtained as a yellowish-brown powder as shown in Figure 2. The possible chemical reaction has also been represented in Figure 3.

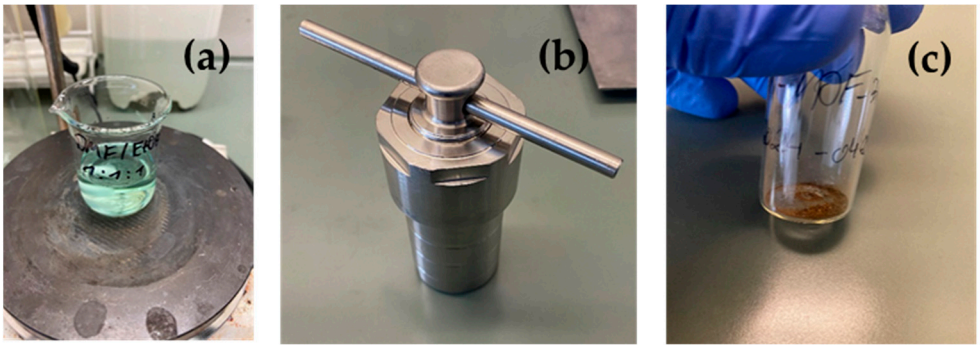

Figure 2. Synthesis of Ni-MOF-74 particles: (**a**) precursor solutions; (**b**) mixing of precursors transferred into an autoclave and placed in an oven for 24 h at 100 °C; (**c**) dried Ni-MOF-74 powder.

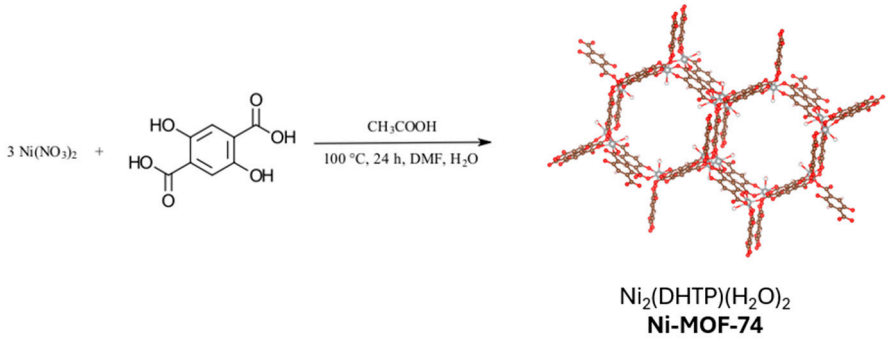

Figure 3. Possible precipitation reaction in Ni-MOF-74 synthesis through solvothermal process.

2.3. Synthesis of NMC622 Through Co-Precipitation Route

As cathode material, NMC622 was synthesized and used. For the synthesis of NMC622, 0.6 mol nickel (II) acetate tetrahydrate ($Ni(CH_3COO)_2$ $4H_2O$), 0.2 mol manganese (II) acetate tetrahydrate ($Mn(CH_3COO)_2$ $4H_2O$), and 0.2 mol cobalt (II) acetate tetrahydrate ($Co(CH_3COO)_2$ $4H_2O$) were each dissolved separately in deionized water. Additionally, 1.5 mol lithium acetate ($LiCH_3COO$) was added to achieve a Li:M ratio of 1.5:1 to compensate for lithium loss during calcination. After mixing all metal precursor solutions under continuous stirring and heating, 1.75 mol of oxalic acid ($C_2H_2O_4$ $2H_2O$) was slowly added dropwise as a co-precipitation agent. The resulting suspension was stirred for 1 h and then heated to 80 °C to reduce the water content. After most of the water content and dried at the same temperature overnight in an oven. The dried precursor was ground using a mortar and subsequently calcined at 850 °C for 8 h in air with a heating rate of 3 °C/min to successfully get the NMC622 powder.

2.4. Fabrication of MOF-Integrated Glass Fiber (GF) Separator

Glass fiber (GF) separators were also coated with the 5 wt% of MOF-polymer solution. Due to the thick and rough surface properties of the glass fiber (GF) separator, it was initially coated using drop casting process (Figure 4). For the preparation of MOF–polymer solution, 1 g of polyvinylidene fluoride (PVDF) was added to 10 mL of acetone in a 20 mL screw cap glass container and stirred on a hot plate at 50 °C for approximately 2 h. After complete dissolution, 5 wt% of MOF relative to PVDF was added to the solution, followed by stirring for an additional 60 min until half of the initially added solvent had evaporated.

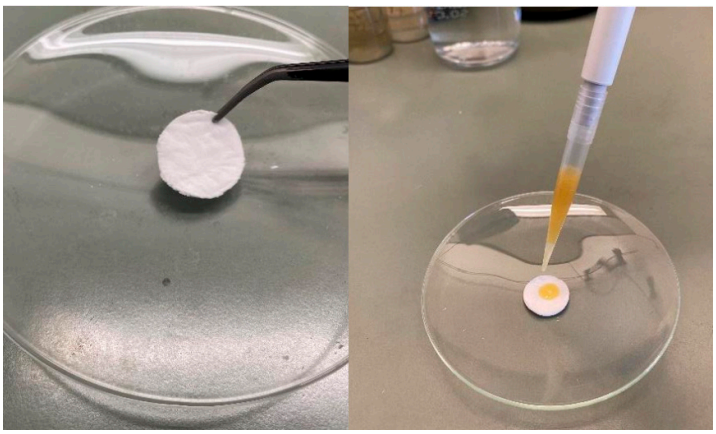

Figure 4. Fabrication of Ni-MOF-74-integrated glass fiber (GF) separator by drop coating process, left is before and right is after drop coating of Ni-MOF-74 into GF.

2.5. Characterizations

The synthesized Zr-MOF-808 and Ni-MOF-74 powder materials have been characterized by various techniques. The crystalline structure and composition of the synthesized Zr-MOF-808 materials are studied using Bruker D8 Advance X-ray diffractometer (XRD, Bruker, Bremen, Germany) under Cu K_α radiation (λ = 1.5406 Å) source, 35 kV voltage and 2θ range of 2–60°. The morphology and size of the MOFs materials have been studied by the scanning electron microscopy (SEM) technique and elemental compositional analysis has been performed by Energy-dispersive X-ray spectroscopy (EDX) with the help of Zeiss Ultra 55 microscopes (Zeiss, Jena, Germany). To investigate the electrochemical performance and suitability for lithium–ion battery (LIB) application, Li-ion coin cell batteries in half-cell form have been initially fabricated and tested using synthesized and commercialNMC622 as cathode, Li-anode, 1 M $LiPF_6$ in EC/DMC (1:1 v/v) (LP30) electrolyte, and various separators such as with and without MOF-integrated glass fiber (GF) separators. Five cycles

galvanostatic charge-discharge (GCD) measurements have been initially carried out to study the electrochemical performance and effect for MOF-integration into the separators. The half-cells LIBs were then also analyzed using electrochemical impedance spectroscopy (EIS). This study significantly helps to investigate the influence of MOF integration on internal resistances in combination with charge transfer and diffusion processes. Finally, the cycle stability of the half cells was tested with the MOF-integrated separators. For this purpose, galvanostatic charging and discharging measurements were started with the cells over 200 cycles.

2.6. Fabrication of NMC622 Cathode for Coin Cell Assembly

Cathodes were produced with synthesised NMC622 as the active material. One of the biggest challenges here was to achieve the right consistency of the slurry so that it can be coated evenly and no cracks or loss of active materials occur during electrode drying after coatings. The best results were achieved in preliminary tests with a PVDF content of 10% as a binding agent. Electrodes were prepared with an 8:1:1 mass ratio of NMC622, activated carbon (AC) and polyvinylidene fluoride (PVDF) binder. First, PVDF was dissolved in the N-Methyl-2-pyrrolidone (NMP) solvent under continuous stirring at 60–65 °C. Afterwards, the PVDF solution was cooled and AC and NMC622 powder were added to the solution followed by stirring of the mixture overnight at a high-speed of 1400 rpm. The resulted slurry was coated on aluminium foil using a doctor blade coating device with a device set up for thickness of 600 µm and dried at 80 °C for 4 h. Finally, 14 mm diameter discs (Figure 5) were punched out from the electrode for assembling the CR2030 half-coin cells. The mass of active material per electrode with a diameter of 14 mm was approx. 15 mg (approx. 9.7 mg cm^{-2}). Subsequently, the assembly of the coin cells was carried out in a glovebox under inert Ar-gas atmosphere and the electrolyte 1M $LiPF_6$ in ethylene carbonate (EC)/dimethyl carbonate (DMC) = 50/50 (*v*/*v*) was used. Commercial NMC622 electrode sheets were also purchased from NEI with 2mAh cm^{-2} capacity loading (approx. 11.11 mg cm^{-2}) and cut into coin-sized electrodes with a diameter of 15 mm. NMC622 half-cells were assembled with Celgard3501, Bare-GF, and Ni-MOF-GF using the same electrolyte composition and Li metal counter electrode.

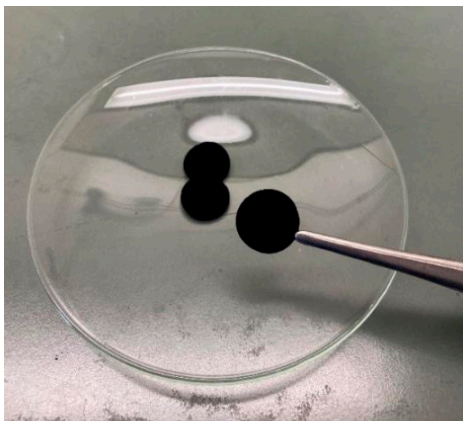

Figure 5. Lithium–nickel–manganese–cobalt–oxide (NMC622) cathodes with a diameter of 14 mm for coin cell assemble.

3. Results and Discussion

The crystal structure of organic frameworks (MOFs) is one of the most important factors for their unique behavior and performance. X-ray diffraction (XRD) analysis indicates that the most important characteristic diffraction peaks (Figure 6a) at 2θ (degree) = 8.36°, 8.78°, 10.08°, and 11.01° are assigned to the planes (311), (222), (400), and (331), respectively

confirming the successful synthesis of crystalline Zr-MOF-808 (JCDPS# 08-0247) [34–36]. The 3D visualization of the crystal lattice of the synthesized Zr-MOF-808 has been created using the powder X-ray diffractogram, as shown in Figure 6a (inset). To confirm the crystallinity, the diffraction peaks of synthesized Ni-MOF-74 powder has also been represented in Figure 6b. The XRD pattern of the synthesized Ni-MOF-74 matches well the patterns in other studies [23,30,37]. The XRD patterns (Figure 6b) of Ni-MOF exhibit two characteristic sharp peaks at around 2θ (degree) = 6.88° and 11.78° that confirms the successful synthesis and formation of crystalline Ni-MOF-74 samples (CCDC No.: 638,866). A 3D visualization of the crystal lattice has also been created using the powder XRD data (Figure 6b (inset)). In contrast to Zr-MOF-808, Ni-MOF-74 has bipyramidal sub boundary units (SBUs) and a honeycomb-like crystal structure that can significantly help to the absorption of gas molecules (such as H_2, CO_2, CH_4, etc.) in these hexagonal free spaces [28,37,38].

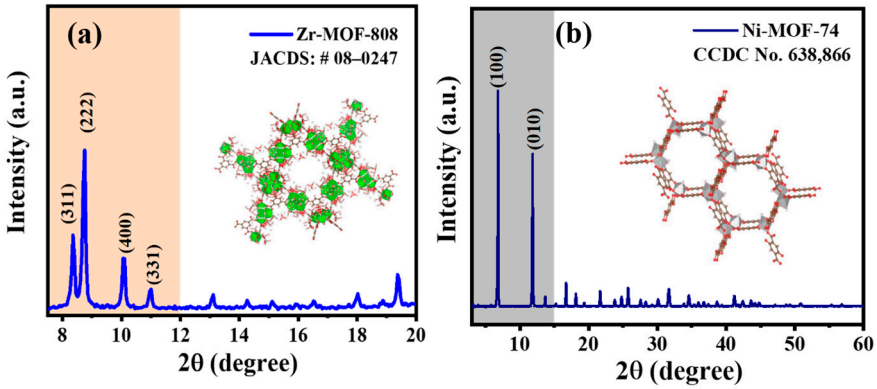

Figure 6. XRD pattern and crystal structure (inset) of synthesized (**a**) Zr-MOF-808 powder and (**b**) Ni-MOF-74 powder materials.

The surface morphology of the synthesized Zr-MOF-808 materials has been observed with SEM investigations as shown in Figure 7. The SEM images in Figure 7a,b show that the smaller size particles agglomerated to form larger spherical secondary particles. It has been observed that the nanosized spherical particle of size range from 50 to 70 nm has been achieved in this cost effective scalable solvothermal synthesis process. Overall, this morphology also indicates that the synthesized Zr-MOF-808 materials possess a high surface area with uniformly distributed porosity that has promising effect on the electrolyte uptake and gas absorption capacity of the materials. The EDX images in Figure 7c,d show that the individual elements are homogeneously distributed and that there is no agglomeration of elemental zirconium or other elements. The surfaces morphology of synthesized Ni-MOF-74 is also shown in Figure 8. The surface morphology of Ni-MOF-74 Figure 8a,b shows a homogeneous distribution of agglomerated particles of relatively bigger sizes of particles. In contrast to the Zr-MOF-808, the SEM images of the synthesized Ni-MOF-74 did not show nanoparticle morphology, but crystalline particles in the micrometre range. The element distribution Figure 8c,d shows that there are no contaminations from impurity atoms. The EDX images also show that the individual elements are evenly distributed and that there is no precipitation of elemental nickel or other elements.

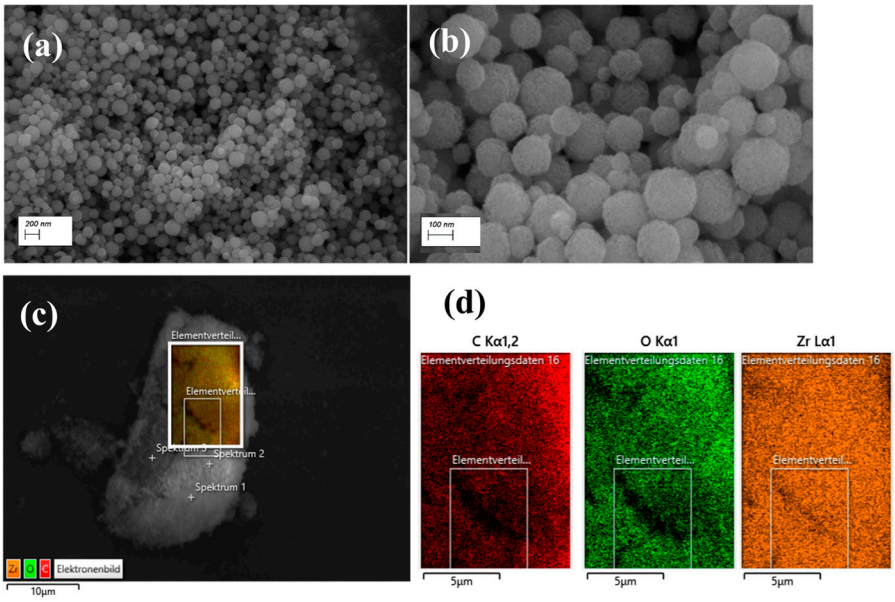

Figure 7. (**a**,**b**) SEM images and (**c**,**d**) EDX images with elemental distribution of synthesized Zr-MOF-808 powder materials.

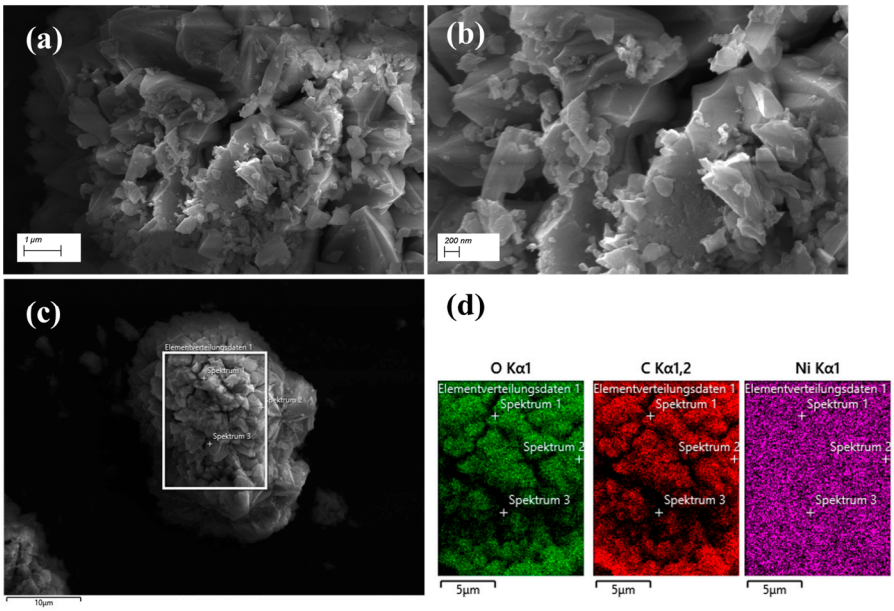

Figure 8. (**a**,**b**) SEM images and (**c**,**d**) EDX images with elemental distribution of synthesized Ni-MOF-74 powder materials.

Glass fiber (GF) separators were also coated with the 5 wt% of Zr-MOF-808 and Ni-MOF-74 polymer solution. Due to the thick and rough surface properties of the GF separator, it was initially coated using drop casting process as shown in Figure 4. The SEM image (Figure 9a) of the uncoated bare GF separator clearly shows the individual micrometre-sized microstructure on the surface of the glass fiber. The SEM images (Figure 9b,c) of the Zr-MOF-808 and Ni-MOF-74-coated GF separators also confirm that the Zr-MOF-808 and Ni-MOF-74 are completely and uniformly integrated into the pores and surface of the glass fiber microstructure. The individual glass fibers are barely visible in Figure 8b,c. Moreover, it can also be seen that the surface of the MOF-integrated GF is porous at nanometer level.

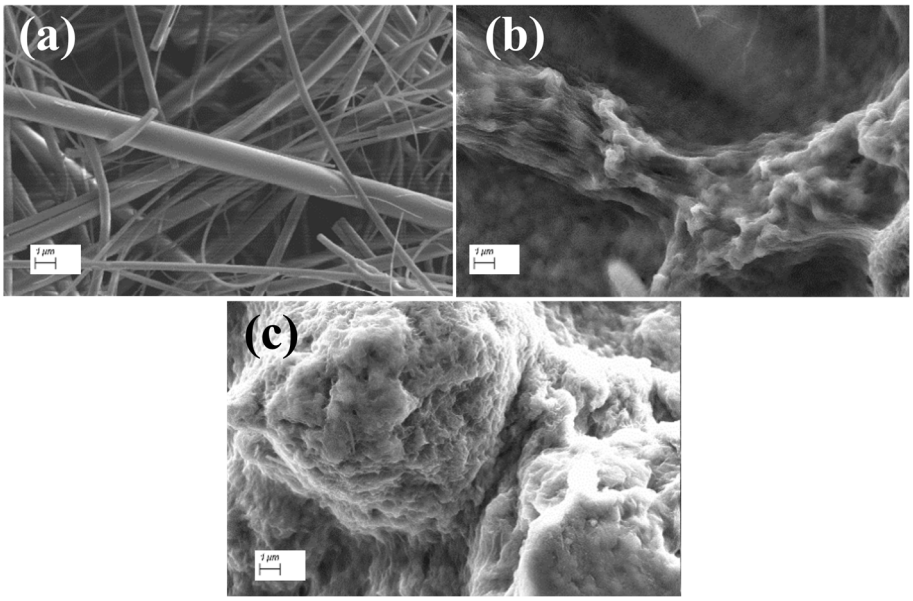

Figure 9. SEM images of (**a**) bare glass fiber (GF) separator, (**b**) 5 wt% Zr-MOF-808-integrated glass fiber (GF) separator and (**c**) 5 wt% Ni-MOF-74-integrated glass fiber (GF) separator.

To further investigate the effect of MOF-integration on GF separators, the charge–discharge measurements of LIBs containing NMC622 cathodes in coin cell form in the voltage range of 2.7 V to 4.2 V at a C/10 current rate for the first five cycles are shown in Figure 10. The charge–discharge curves (Figure 10a) of the LIB with bare glass fiber (GF) separators show a high specific capacity of 109.4 mAh/g for the first discharge cycle. After the fifth cycle, the specific capacity of this cell increased slightly to 115.9 mAh/g, which may be due to electrochemical activation of the electrode materials and sometimes common for NMC cathodes during the early aging stage, known as initial capacity increase [39–41]. The charge–discharge curves of the LIB cell composed of 5 wt% Zr-MOF-808-integrated GF separator (Figure 10b) shows that the overall capacity increases to 134.5 mAh/g in the first discharge cycle and after the fifth cycle it maintains a nearly constant capacity at around 127.1 mAh/g, with a very low capacitance loss of 7.4 mAh/g. Similarly, the LIB cell composed of 5 wt% Ni-MOF-74-integrated GF separator also exhibits an initial discharge capacity of 145.2 mAh/g and 139.2 mAh/g after the fifth cycle. However, initial capacity loss in the first charge–discharge cycle is observed for both MOF-integrated separator-based LIBs which is mainly due to the formation of electrolyte decomposition products and the formation of solid electrolyte interphase (SEI) film [42,43]. Typically, even high-capacity layered NMC cathode experience irreversible capacity loss in the first charge–discharge cycle. Low initial coulombic efficiency of NMC cathodes is referred to the irreversible loss of Li_2O from Li_2MnO_3 region [44]. However, optimal thickness and porous surface of the GF-separators significantly improve the MOF-integration and capacity of the LIB cells. Both MOFs (Zr-MOF-808 and Ni-MOF-74) significantly improve electrolyte uptake and facilitate the movement of Li^+ ions through the GF-separators, resulting in increased capacity and increased stability of the cell performance [6,45].

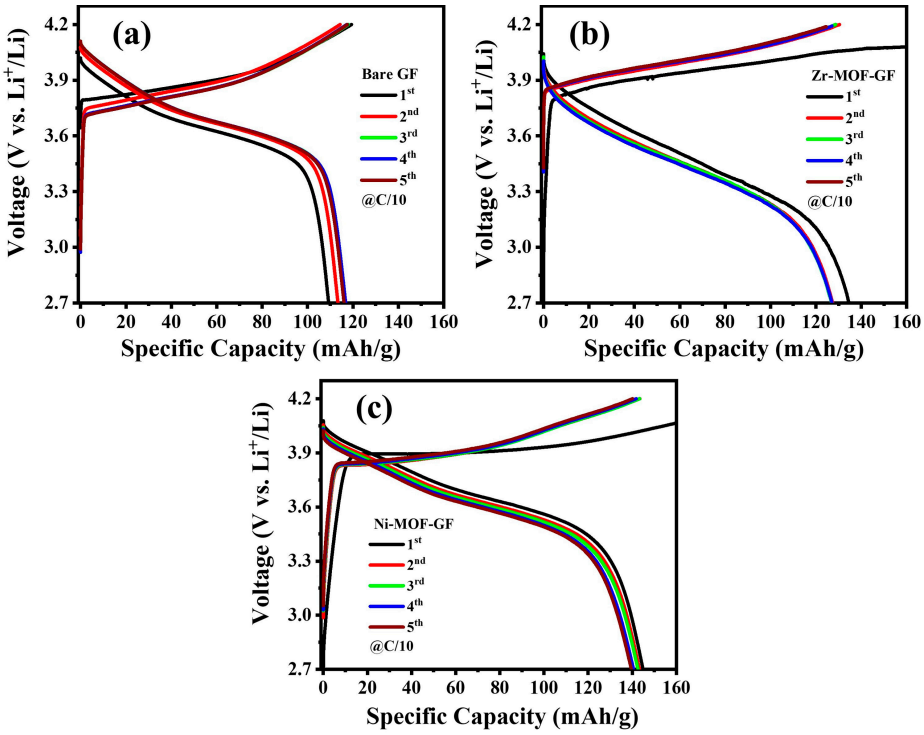

Figure 10. GCD measurements of lithium–ion half-cells with NMC 622 cathode and (**a**) bare glass fiber (GF) separators, (**b**) 5wt% Zr-MOF-808-integrated glass fiber (GF) separators, and (**c**) 5wt% Ni-MOF-74-integrated glass fiber (GF) separators in a voltage window of 2.7–4.2 V.

The electrochemical impedance spectroscopy (EIS) analysis in term of the Nyquist plots of bare GF-separator and MOF-integrated GF-separator based coin cell lithium–ion battery have been carried out at room temperature in the frequency range of 100 kHz to 0.01 Hz with a.c. amplitude of 5 mV. Two EIS curves in Figure S1 show a depressed semicircle consisting of two semicircles at high frequencies and a notable diffusion tail at low frequencies. All EIS curves in terms of Nyquist plots have been fitted with equivalent circuit model using EC-Lab software. The equivalent circuit in Figure S1 (inset) reveals that R_s represents the electrolyte resistance and contact resistance of electrode/current collector, the first semicircle at high frequencies corresponding to the cathode–electrolyte interface (R_{CEI} and CPE_{CEI}), the second semicircle at medium frequencies corresponding to the charge-transfer (R_{ct}) behavior of the electrode and the sloping line in the low frequencies signifies the Li^+ ions diffusion (Warburg diffusion, $W_{Warburg}$) into the cathode [46–49]. There is a significant change in overall cell impedance values observed after use of MOF-integrated GF separators. The R_{ct} value changes from 43.2 Ω to 24.3 Ω for Zr-MOF-GF separator and 14.9 Ω for Ni-MOF-GF separators, respectively, indicating faster ion transfer kinetics. This suggests that the MOF integration into the separator facilitate effective and continuous conducting pathways for ions [7,37,50–52]. Moreover, this outcome can be attributed to the characteristic properties of Zr-MOF and Ni-MOF, such as their synergistic physical, ionic transport conductivity, and large surface area, which can facilitate Li^+ ions transfer between the electrode and the electrolyte [14,33,53].

To obtain more clear information about the stability of the battery performance, a comparative long cycle study for 50 cycles at C/10 within the same voltage range of 2.7 and 4.2 V has been conducted for both LIB cells composed of Zr-MOF-808-integrated GF-separator and bare GF-separator. For NMC622 cathode and bare GF-separator-based cell shows (Figure S2a) initial discharge capacity of 109.4 mAh/g and reduced to the value of 72.6 mAh/g after 50th cycle. The Zr-MOF-808-integrated GF-separator (Figure S2b) and Ni-MOF-74-integrated GF-separator (Figure S2c)-based LIB show good capacity retention

after 50 cycles. They offer capacity of 84.3 mAh/g for Zr-MOF and 96.6 mAh/g for Ni-MOF in the first cycle and reduced to 72.3 mAh/g for Zr-MOF and 94.1 mAh/g for Ni-MOF after end of 50 cycles, which indicates the stable performance of the MOF-integrated separator-based LIBs. Based on the slow cycling data of MOF-integrated GF separator results, the Ni-MOF-GF separator was selected for the GCD test under a higher C-rate (1C).

A commercial NMC622 electrode with 15 mm diameter was assembled with various kinds of separators to evaluate the produced MOF performance. LP30 (1M LiPF6 EC:DMC (1:1 v/v)) electrolyte and Li metal as counter and reference electrode were used to assemble the half-cells. The system was not restricted by any time or capacity except the upper-cutoff voltage during charge at formation cycles to be able to produce as much gas as possible. The first formation cycles showed that electrodes performed over 210 mAh/g specific capacity during charging, which was higher than NMC622's approximate capacity of around 180 mAh/g, leading to overcharging of the cell until 4.2V (Figure 11a). Commercial NMC622 electrodes with bare-Celgard, bare-GF (0 wt% Ni-MOF-GF), and 5 wt% Ni-MOF-GF separators performed almost identical discharge capacities of 173 mAh/g under CCCV discharge conditions. The cells were subjected to galvanostatic charge–discharge (GCD) test for long-term stability performance investigation (Figure 11b). It was found that, NMC622 cell with bare-Celgard 3501 separator (black line) showed the poor performance with losing more than 80% of starting capacity after 50 cycles during cycling at 1C. In the first 50 cycles bare-GF separator cell (red line) and 5 wt% Ni-MOF-GF separator cell (blue line) performed similar behavior. However, cell performance of 5 wt% Ni-MOF-GF separator started to decrease more than bare-GF in next 100 cycles. The most critical part was after 150th cycle bare-GF cell lost its 66% of capacity in 10 cycles, while the degradation of 5 wt% Ni-MOF-GF separator showed more reliable performance. The LIB cell composed of bare-GF separator (Figure 11b) exhibits a higher initial capacity retention compared to the cell with 5 wt% Ni-MOF-integrated GF-separators because it offers an unobstructed pathway for ions, but it experiences rapid degradation due to unregulated dendrite growth and chemical degradation. Conversely, the cell composed of 5 wt% Ni-MOF-integrated GF-separator requires a few initial cycles to overcome a minor initial resistance, but its ability to regulate ion flow and protect the battery chemistry ensures far superior long-term capacity retention. These results also indicate that the MOF material likely adsorbed the generated gas, which had previously hindered the movement of lithium–ions and suppressed cell capacity [54–56]. However, due to the absence of any absorbing agent in bare-GF, the lithium metal started to passivate through reactions with the gas over 150 cycles, which can be observed from the sharp decline in its capacity compared to the 5 wt% Ni-MOF-GF separator cells. The cells were subjected to a cycling test under a slow C-rate (0.1C) for cells' degradation evaluation. The results showed that the 5 wt% Ni-MOF-GF separator cell retains 81.5% of its original capacity after 200 cycles of GCD at 1C (Figure 11c). The bare-Celgard and bare-GF cells have lost more than 50% of their original capacity. These results demonstrate that impregnating the separator with MOF to absorb the generated gases helps extend the lifespan and performance of the cells.

EIS results showed that commercial NMC622 cells had a similar impedance value before the GCD test began (Table 1 and Figure S3). EIS measurements of the cells were repeated after 200 cycles of the GCD test. The results indicate that the GF separator impregnated with 5 wt% Ni-MOF inhibited cell degradation by adsorbing the gases generated because of electrolyte decomposition and SEI formation. Based on the impedance results, the 5 wt% Ni-MOF-GF separator cell inhibited the electrode degradation, corresponding to an increase of less charge transfer resistance compared to bare-Celgard and bare-GF cells. Moreover, XRD analysis was performed on GF separators to monitor the changes (Figure S4). It was found that the fresh bare-GF separator showed broad intensity in be-

tween 2θ (Mo K_α) 7–14°. On the other hand, 5 wt% Ni-MOF-GF showed a quasi-crystalline structure with two peaks observed at 2θ = 3.94° and 9.21°. The 2θ = 3.94° peak disappeared after 200 cycles, which may correspond to 5 wt% Ni-MOF-GF gas trapping.

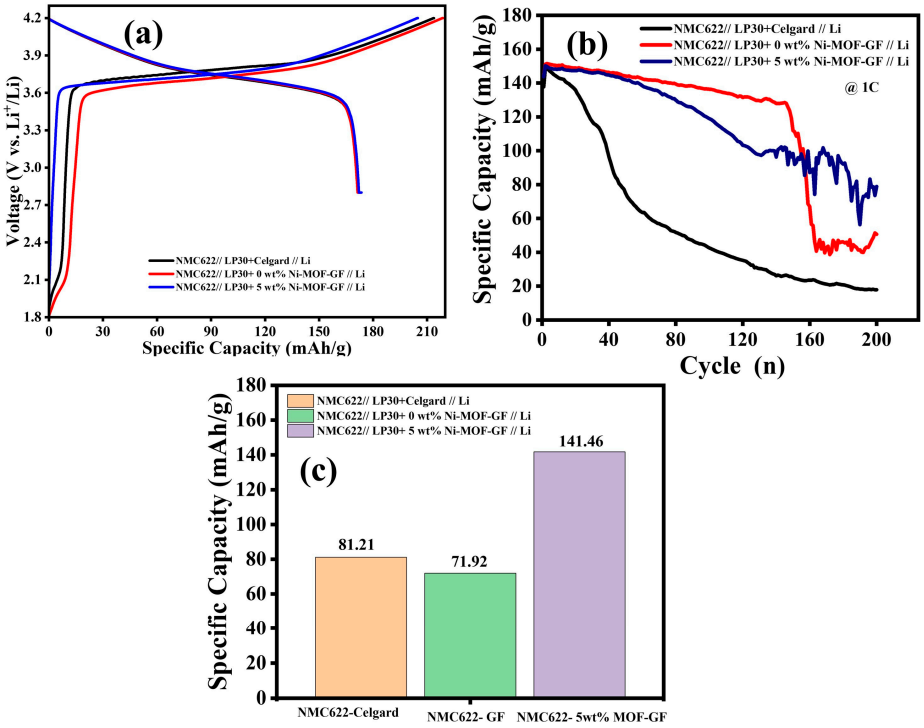

Figure 11. Comparative analysis of bare-Celgard3501, bare-GF, and 5wt% Ni-MOF-GF separators in the voltage range of 2.8–4.2 V (**a**) Formation cycle of commercial NMC622 half cells, (**b**) long-term GCD cycles at 1C for 200 cycles, (**c**) capacitance analysis of NMC622.

Table 1. EIS calculation of commercial NMC622 half-cell with bare-Celgard, bare-GF, and 5 wt% Ni-MOF-GF separators.

	Before GCD			After GCD		
	Celgard	**Bare-GF**	**Ni-MOF-GF**	**Celgard**	**Bare-GF**	**Ni-MOF-GF**
R_b	1.964	3.21	5.145	20.516	50.547	113.275
R_{ct}	3.28	3.162	3.666	129.347	164.00	41.284
W	198.555	145.121	148.271	626.706	358.362	125.283

4. Conclusions

The main aim of this research work is to describe the details of metal organic frameworks (MOFs) synthesis, the fabrication of separators composed of synthesized MOFs and their performance. The synthesis parameters have been established for the synthesis of nanostructured Zr-MOF-808 and Ni-MOF-74 materials via a facile process-controlled solvothermal method. These MOFs have been successfully integrated into glass fiber (GF) separators. Both MOF-integrated separators based half-cells showed significantly lower cell resistance compared with bare GF-separator. These extensive studies confirmed that MOFs can be used to modify the surface and porosity of separators. The results indicate that the integration of Zr-MOF-808 and Ni-MOF-74 increased the surface area and overall porosity of the separators, resulting in improved wettability and electrolyte uptake capacity. Additionally, the MOF-integrated separators reduced the electrochemical resistance of the separators and at the separator-electrolyte interfaces. The MOF materials into the

separators also increase the reaction kinetics, improving ionic/electrical conductivity and provide favorable channels for ion transport. In general, it is assumed that the capacity losses during the long cycle are due to degradation of the battery components such as the cathode, anode, or the electrolyte. This degradation is caused by unwanted side reactions such as the production of insoluble lithium oxide (LiO_2) and the evaluation of various gases such as H_2, O_2, CO, CO_2, and H_2O. Typical separators also induce several problems such as insufficient thermal stability and susceptibility to crystal branching. The MOF-integrated separators developed in this work possess high structural stability and provide stable ion transport pathways, thus reducing the probability of degradation and increasing the cell lifetime and electrochemical stability. The studies will be extended to analyses their characteristics to absorb the gases inside the cell. This requires a more intensive optimization of MOF-integrated separator fabrication, establishment of gas absorption ability which makes the content of the upcoming experiments. This study opens new directions in research to reduce battery performance degradation. Overall, the electrochemical studies done so far confirmed that the MOF-integrated separators function excellently to improve the battery performance yielding a promising component for the next generation of battery production.

Supplementary Materials: The following supporting information can be downloaded at: https://www.mdpi.com/article/10.3390/batteries12060218/s1, Figure S1: Electrochemical impedance spectroscopy (EIS) curves with equivalent circuit model (inset) for Bare GF, Zr-MOF-GF and Ni-MOF-GF separator-based LIBs; Figure S2: Charge discharge curve for 50 cycles at C/10 for (a) without MOF-integrated GF-separator based LIB, (b) Zr-MOF-808 integrated GF-separator and (c) Ni-MOF-74 integrated GF-separator based LIB; Figure S3: Nyquist graph comparison of commercial NMC622 half-cells with Celgard, Bare-GF, and Ni-MOF-GF (a) Before GCD and (b) after GCD; Figure S4: XRD graphs of (a) Fresh Bare-GF and Bare-GF after 200 cycles, (b) Fresh Ni-MOF-GF and Ni-MOF-GF after 200 cycles.

Author Contributions: Conceptualization, A.R. and B.S.; methodology, A.R. and N.W.; validation, A.R., N.W., E.G., B.T., K.B.D. and B.S.; formal analysis, N.W.; investigation, N.W., A.R. and E.G.; resources, B.S.; data curation, A.R., N.W. and E.G.; writing—original draft preparation, A.R.; writing—review and editing, B.S., B.T., N.W., E.G., K.B.D. and M.B.; visualization, A.R.; supervision, B.S.; project administration, B.S.; funding acquisition, B.S. All authors have read and agreed to the published version of the manuscript.

Funding: This project has received funding from the European Union's research and innovation program Horizon Europe under the grant agreement No. 101103702 (PHOENIX) and the involvement in No. 101104022 (Battery 2030 CSA3). Views and opinions expressed are, however, those of the author(s) only and do not necessarily reflect those of the European Union. Neither the European Union nor the granting authority can be held responsible for them.

Data Availability Statement: Data will be made available on request.

Acknowledgments: The authors A. Ray, N. Wood, E. Guney, B. Tasdemir, K. B. Dermenci, M. Berecibar and B. Saruhan are grateful to the European Union's research and innovation programme Horizon Europe under the grant agreement No. 101103702 and the involvement in No. 101104022 (Battery 2030 CSA3) for financial support in the frame of projects PHOENIX.

Funded by
the European Union

Conflicts of Interest: The authors declare no conflicts of interest.

References

1. Davis, K.; Demopoulos, G.P. Effective upcycling of NMC 111 to NMC 622 cathodes by hydrothermal relithiation and Ni-enriching annealing. *Next Energy* **2024**, *4*, 100122. [CrossRef]
2. Li, Q.; Chen, J.; Fan, L.; Kong, X.; Lu, Y. Progress in electrolytes for rechargeable Li-based batteries and beyond. *Green Energy Environ.* **2016**, *1*, 18–42. [CrossRef]
3. Mayanti, B.; Azemtsop, T.; Hafiz, M.; Nebiyu, H.; Jonas, G. Environmental and economic assessment of bio-based anode production. *Clean Technol. Environ. Policy* **2026**, *28*, 149. [CrossRef]
4. Chen, X.; Wang, Z.; Wang, J.; Lin, Y.; Li, J. Impact of Low-Pressure in High-Altitude Area on the Aging Characteristics of NCM523/Graphite Pouch Cells. *Batteries* **2025**, *11*, 261. [CrossRef]
5. Liu, W.; Chen, G.; Wang, N.; Sun, X.; Li, C.; Xu, Y.; Zhang, X.; Zhang, X.; Wang, K. Tetramethylene Sulfone (TMS) as an Electrolyte Additive for High-Power Lithium-Ion Batteries. *Batteries* **2025**, *11*, 270. [CrossRef]
6. Deng, L.; Cai, C.; Huang, Y.; Fu, Y. In-situ MOFs coating on 3D-channeled separator with superior electrolyte uptake capacity for ultrahigh cycle stability and dendrite-inhibited lithium-ion batteries. *Microporous Mesoporous Mater.* **2022**, *329*, 111544. [CrossRef]
7. Liu, X.; Wu, Y.; Yang, F.; Wang, S.; Zhang, B.; Wang, L. An effective dual-channel strategy for preparation of polybenzimidazole separator for advanced-safety and high-performance lithium-ion batteries. *J. Memb. Sci.* **2021**, *626*, 119190. [CrossRef]
8. Alawi, A.; Saeed, A.; Sharqawy, M.H.; Al Janaideh, M. A Comprehensive Review of Thermal Management Challenges and Safety Considerations in Lithium-Ion Batteries for Electric Vehicles. *Batteries* **2025**, *11*, 275. [CrossRef]
9. Rowden, B.; Garcia-Araez, N. A review of gas evolution in lithium ion batteries. *Energy Rep.* **2020**, *6*, 10–18. [CrossRef]
10. Mattinen, U.; Klett, M.; Lindbergh, G.; Wreland Lindström, R. Gas evolution in commercial Li-ion battery cells measured by on-line mass spectrometry–Effects of C-rate and cell voltage. *J. Power Sources* **2020**, *477*, 228968. [CrossRef]
11. Bartsch, T.; Strauss, F.; Hatsukade, T.; Schiele, A.; Kim, A.Y.; Hartmann, P.; Janek, J.; Brezesinski, T. Gas Evolution in All-Solid-State Battery Cells. *ACS Energy Lett.* **2018**, *3*, 2539–2543. [CrossRef]
12. Mahne, N.; Schafzahl, B.; Leypold, C.; Leypold, M.; Grumm, S.; Leitgeb, A.; Strohmeier, G.A.; Wilkening, M.; Fontaine, O.; Kramer, D.; et al. Singlet Oxygen Generation as a Major Cause for Parasitic Reactions during Cycling of Aprotic Lithium-Oxygen Batteries. *Nat. Energy* **2017**, *2*, 17036. [CrossRef]
13. Li, Y.; Shi, B.; Liu, W.; Guo, R.; Pei, H.; Ye, D.; Xie, J.; Kong, J. Hollow polypyrrole @ MnO_2 spheres as nano-sulfur hosts for improved lithium-sulfur batteries. *Electrochim. Acta* **2018**, *260*, 912–920. [CrossRef]
14. Davino, S.; Callegari, D.; Pasini, D.; Thomas, M.; Nicotera, I.; Bonizzoni, S.; Mustarelli, P.; Quartarone, E. Cross-Linked Gel Electrolytes with Self-Healing Functionalities for Smart Lithium Batteries. *ACS Appl. Mater. Interfaces* **2022**, *14*, 51941–51953. [CrossRef] [PubMed]
15. Tasdemir, B.; Krüger, S.; Sohagiya, P.; Ray, A.; Saruhan, B. Improvement of Cycling Stability of Core–Shell Structured Ni-Rich NMC Cathodes by Using a Tungsten Oxide Stabilization Interlayer. *Batteries* **2026**, *12*, 82. [CrossRef]
16. Hamed, S.; Obrezkov, F.; Huotari, S.; Colalongo, M.; Mousavihashemi, S.; Kallio, T. Optimized NMC622 electrodes with a high content of the active material: A comprehensive study. *J. Power Sources* **2024**, *608*, 234549. [CrossRef]
17. Strauss, F.; Teo, J.H.; Schiele, A.; Bartsch, T.; Hatsukade, T.; Hartmann, P.; Janek, J.; Brezesinski, T. Gas Evolution in Lithium-Ion Batteries: Solid versus Liquid Electrolyte. *ACS Appl. Mater. Interfaces* **2020**, *12*, 20462–20468. [CrossRef] [PubMed]
18. Li, T.; Yuan, X.Z.; Zhang, L.; Song, D.; Shi, K.; Bock, C. Degradation Mechanisms and Mitigation Strategies of Nickel-Rich NMC-Based Lithium-Ion Batteries. *Electrochem. Energ. Rev.* **2020**, *3*, 43–80. [CrossRef]
19. Agubra, V.A.; Fergus, J.W. The formation and stability of the solid electrolyte interface on the graphite anode. *J. Power Sources* **2014**, *268*, 153–162. [CrossRef]
20. Zhao, T.; Xiao, P.; Nie, S.; Luo, M.; Zou, M.; Chen, Y. Recent progress of metal-organic frameworks based high performance batteries separators: A review. *Coord. Chem. Rev.* **2024**, *502*, 215592. [CrossRef]
21. Wade, T.L. *High Power Carbon Based Supercapacitors*; University of Melbourne, School of Chemistry: Parkville, VIC, Australia, 2006; pp. 47–142.
22. Kerner, M.; Johansson, P. Pyrrolidinium fsi and TFSI-based polymerized ionic liquids as electrolytes for high-temperature lithium-ion batteries. *Batteries* **2018**, *4*, 10. [CrossRef]
23. Qu, C.; Zhao, B.; Jiao, Y.; Chen, D.; Dai, S.; Deglee, B.M.; Chen, Y.; Walton, K.S.; Zou, R.; Liu, M. Functionalized Bimetallic Hydroxides Derived from Metal-Organic Frameworks for High-Performance Hybrid Supercapacitor with Exceptional Cycling Stability. *ACS Energy Lett.* **2017**, *2*, 1263–1269. [CrossRef]
24. Mehek, R.; Iqbal, N.; Noor, T.; Amjad, M.Z.B.; Ali, G.; Vignarooban, K.; Khan, M.A. Metal-organic framework based electrode materials for lithium-ion batteries: A review. *RSC Adv.* **2021**, *11*, 29247–29266. [CrossRef] [PubMed]
25. Wang, W.; Chen, D.; Li, F.; Xiao, X.; Xu, Q. Metal-organic-framework-based materials as platforms for energy applications. *Chem* **2024**, *10*, 86–133. [CrossRef]
26. Cheng, Z.; Lian, J.; Zhang, J.; Xiang, S.; Chen, B.; Zhang, Z. Pristine MOF materials for separator application in lithium–sulfur battery. *Adv. Sci.* **2024**, *11*, 2404834. [CrossRef] [PubMed]

27. Zheng, X.; Fang, H.; Wan, Y.; Zhang, X.; Zhang, Y.; Hirunpinyopas, W.; Wu, M.; Wang, B. Recent advances in MOF-based functional separators for lithium-metal/lithium-sulfur batteries. *Coord. Chem. Rev.* **2026**, *552*, 217512. [CrossRef]
28. Zhang, X.; Zheng, Q.R.; He, H.Z. Multicomponent adsorptive separation of CO_2, CH_4, N_2, and H_2 over M-MOF-74 and AX-21@M-MOF-74 composite adsorbents. *Microporous Mesoporous Mater.* **2022**, *336*, 111899. [CrossRef]
29. Razaq, R.; Mehraj, M.; Din, U.; Småbråten, D.R.; Eyupoglu, V.; Janakiram, S.; Sunde, T.O.; Allahgoli, N.; Rettenwander, D. Synergistic Effect of Bimetallic MOF Modified Separator for Long Cycle Life Lithium-Sulfur Batteries. *Adv. Energy Mater.* **2024**, *14*, 2302897. [CrossRef]
30. Park, B.H.; Jung, Y.; Kim, S. Particle Size Control Influence on the Electrochemical Properties of Sulfur Deposited on Metal Organic Frameworks Host Electrodes. *J. Inorg. Organomet. Polym. Mater.* **2021**, *31*, 1931–1938. [CrossRef]
31. Kevat, S.; Lad, V.N. Green synthesis of zirconium-based MOF-808 by utilizing sustainable synthesis approaches. *J. Organomet. Chem.* **2023**, *999*, 122832. [CrossRef]
32. Wang, K.; Wang, Z.; Wang, X.; Zhou, X.; Tao, Y.; Wu, H. Flexible long-chain-linker constructed Ni-based metal-organic frameworks with 1D helical channel and their pseudo-capacitor behavior studies. *J. Power Sources* **2018**, *377*, 44–51. [CrossRef]
33. Jin, Z.; Li, Y.; Ma, Q. CoAl LDH@Ni-MOF-74 S-Scheme Heterojunction for Efficient Hydrogen Evolution. *Trans. Tianjin Univ.* **2021**, *27*, 127–138. [CrossRef]
34. Zhang, X.; Yu, R.; Wang, D.; Li, W.; Zhang, Y. Green Photocatalysis of Organic Pollutants by Bimetallic Zn-Zr Metal-Organic Framework Catalyst. *Front. Chem.* **2022**, *10*, 918941. [CrossRef] [PubMed]
35. Liu, H.; Zhao, Y.; Zhou, C.; Mu, B.; Chen, L. Microwave-assisted synthesis of Zr-based metal–organic framework (Zr-fum-fcu-MOF) for gas adsorption separation. *Chem. Phys. Lett.* **2021**, *780*, 138906. [CrossRef]
36. Sharifi-Rad, M.; Kaykhaii, M.; Khajeh, M.; Oveisi, A. Synthesis, characterization and application of a zirconium-based MOF-808 functionalized with isonicotinic acid for fast and efficient solid phase extraction of uranium(VI) from wastewater prior to its spectrophotometric determination. *BMC Chem.* **2022**, *16*, 27. [CrossRef] [PubMed]
37. Wang, S.; Guo, Q.; Liang, S.; Li, P.; Luo, J. Preparation of Ni-MOF-74/SBS mixed matrix membranes and its application of CH_4/N_2 separation. *Sep. Purif. Technol.* **2018**, *199*, 206–213. [CrossRef]
38. Lee, D.J.; Li, Q.; Kim, H.; Lee, K. Preparation of Ni-MOF-74 membrane for CO_2 separation by layer-by-layer seeding technique. *Microporous Mesoporous Mater.* **2012**, *163*, 169–177. [CrossRef]
39. Guo, J.; Li, Y.; Meng, J.; Pedersen, K.; Gurevich, L.; Stroe, D.I. Understanding the mechanism of capacity increase during early cycling of commercial NMC/graphite lithium-ion batteries. *J. Energy Chem.* **2022**, *74*, 34–44. [CrossRef]
40. Dose, W.M.; Morzy, J.K.; Mahadevegowda, A.; Ducati, C.; Grey, C.P.; De Volder, M.F.L. The influence of electrochemical cycling protocols on capacity loss in nickel-rich lithium-ion batteries. *J. Mater. Chem. A* **2021**, *9*, 23582–23596. [CrossRef] [PubMed]
41. Jasielec, J.J.; Peljo, P. Limitations of Fast Charging of High Energy NMC-based Lithium-Ion Batteries: A Numerical Study. *Batter. Supercaps* **2023**, *6*, e202300189. [CrossRef]
42. Wang, A.; Kadam, S.; Li, H.; Shi, S.; Qi, Y. Review on modeling of the anode solid electrolyte interphase (SEI) for lithium-ion batteries. *NPJ Comput. Mater.* **2018**, *4*, 15. [CrossRef]
43. Jung, R.; Linsenmann, F.; Thomas, R.; Wandt, J.; Solchenbach, S.; Maglia, F.; Stinner, C.; Tromp, M.; Gasteiger, H.A. Nickel, Manganese, and Cobalt Dissolution from Ni-Rich NMC and Their Effects on NMC622-Graphite Cells. *J. Electrochem. Soc.* **2019**, *166*, A378–A389. [CrossRef]
44. Pan, T.; Alvarado, J.; Zhu, J.; Yue, Y.; Xin, H.L.; Nordlund, D.; Lin, F.; Doeff, M.M. Structural Degradation of Layered Cathode Materials in Lithium-Ion Batteries Induced by Ball Milling. *J. Electrochem. Soc.* **2019**, *166*, A1964–A1971. [CrossRef]
45. Zheng, S.; Ma, J.; Fang, K.; Li, S.; Qin, J.; Li, Y.; Wang, J.; Zhang, L.; Zhou, F.; Liu, F.; et al. High-Voltage Potassium Ion Micro-Supercapacitors with Extraordinary Volumetric Energy Density for Wearable Pressure Sensor System. *Adv. Energy Mater.* **2021**, *11*, 2003835. [CrossRef]
46. Frankenberger, M.; Singh, M.; Dinter, A.; Pettinger, K.H. EIS study on the electrode-separator interface lamination. *Batteries* **2019**, *5*, 71. [CrossRef]
47. Zhu, P.; Ebert, B.; Smyrek, P.; Pfleging, W. The Impact of Structural Pattern Types on the Electrochemical Performance of Ultra-Thick NMC 622 Electrodes for Lithium-Ion Batteries. *Batteries* **2024**, *10*, 58. [CrossRef]
48. Abbas, I.; Tran, H.T.; Tran, T.T.N.; Pham, T.L.; Shin, E.-C.; Park, C.-W.; Yu, S.-B.; Lee, O.J.; Nguyen, A.-G.; Jeong, D.; et al. GITT Limitations and EIS Insights into Kinetics of NMC622. *Batteries* **2025**, *11*, 234. [CrossRef]
49. Loghavi, M.M.; Nahvibayani, A.; Moghim, M.H.; Babaiee, M.; Baktashian, S.; Eqra, R. Electrochemical evaluation of $LiNi_{0.5}Mn_{0.3}Co_{0.2}O_2$, $LiNi_{0.6}Mn_{0.2}Co_{0.2}O_2$, and $LiNi_{0.8}Mn_{0.1}Co_{0.1}O_2$ cathode materials for lithium-ion batteries: From half-coin cell to pouch cell. *Monatshefte Fur Chem.* **2022**, *153*, 1197–1212. [CrossRef]
50. Liu, Q.; Wang, B.; Chen, J.; Li, F.; Liu, K.; Wang, Y.; Li, M.; Lu, Z.; Wang, W.; Wang, D.; et al. Facile synthesis of three-dimensional (3D) interconnecting polypyrrole (PPy) nanowires/nanofibrous textile composite electrode for high performance supercapacitors. *Compos. Part A Appl. Sci. Manuf.* **2017**, *101*, 30–40. [CrossRef]

51. Ray, A.; Roy, A.; Ghosh, M.; Ramos-ramón, J.A.; Saha, S. Applied Surface Science Study on charge storage mechanism in working electrodes fabricated by sol-gel derived spinel $NiMn_2O_4$ nanoparticles for supercapacitor application. *Appl. Surf. Sci.* **2019**, *463*, 513–525. [CrossRef]
52. Sandhu, Z.A.; Raza, M.A.; Awwad, N.S.; Ibrahium, H.A.; Farwa, U.; Ashraf, S.; Dildar, A.; Fatima, E.; Ashraf, S.; Ali, F. Metal–organic frameworks for next-generation energy storage devices; a systematic review. *Mater. Adv.* **2024**, *5*, 30–50. [CrossRef]
53. Nakatsuka, K.; Yoshii, T.; Kuwahara, Y.; Mori, K.; Yamashita, H. Controlled Pyrolysis of Ni-MOF-74 as a Promising Precursor for the Creation of Highly Active Ni Nanocatalysts in Size-Selective Hydrogenation. *Chem.–A Eur. J.* **2018**, *24*, 898–905. [CrossRef]
54. Wang, X.; Du, Z.; Tang, H.; Yu, W.; Liu, T. Metal-organic frameworks and derivatives as next-generation materials for electrochemical energy storage. *Mater. Horiz.* **2026**, *13*, 1227–1260. [CrossRef] [PubMed]
55. Lu, W.; Xu, Y.; Dazon, C.; Macaulay, F.; Pimenta, V.; Serre, C. MOF and related composites as selective functional separators and interlayers for Li-S batteries. *Energy Mater.* **2025**, *5*, 500075. [CrossRef]
56. Zhao, T.; Bi, Y.; Chen, J.; Yu, J.; Peng, S.; Luo, F.; Chen, Y. Progress in Improving Safety Performance of Battery Separators Based on MOF Materials: Mechanisms, Materials and Applications. *Safety* **2025**, *11*, 111. [CrossRef]